IOP Publishing Physica Scripta
Phys. Scr. 95 (2020) 055508 (9pp) https://doi.org/10.1088/1402-4896/ab7b09

Characterization of off-axis phase singular optical vortex and its nonlinear wave-mixing to generate control broad OAM spectra

A Srinivasa Rao

School of Physical Science and Technology, Soochow University, Suzhou 215006, People's Republic of China

E-mail: asrao@suda.edu.cn and sri.jsp7@gmail.com

Received 6 October 2019, revised 27 February 2020
Accepted for publication 28 February 2020
Published 13 March 2020

Abstract

We theoretically and numerically studied the off-axis Gaussian vortex beam (GVB) characteristics. The off-axis GVB scheme is utilized to generate tunable broad OAM modes using a single helical phase. The single helical phase can be easily created in the high peak power lasers using a spiral phase plate (SPP). The high peak power GVBs greatly enhances the efficiency of nonlinear wave-mixing to tune the wavelength as well as OAM modes of laser beams. Further, we propose type-II second harmonic generation (SHG) of off-axis GVB to tune the wavelength and to increase the number of OAM modes of vortex beam. Polarization-controlled broad OAM spectra is generated at SHG wavelength. This scheme is effective for control generation of a broad range of OAM spectra in the required wavelength for high-capacity and multi-channel optical communication.

Keywords: nonlinear wave-mixing, OAM spectra, off-axis Gaussian vortex beam, type-II SHG

(Some figures may appear in colour only in the online journal)

1. Introduction

In 1992, orbital angular momentum (OAM) first introduced and quantified by Allen in the optical beams [1]. The OAM in the optical beams provide the extra degree of freedom to the polarization and has extended the basis of optical beams for high capacity optical communication. The OAM carrying optical beams proved to be a powerful tool for super dense data encoding and decoding in the information processing [2–4]. Further, the entanglement of photons through their OAM properties has established secure quantum information processing [5–7]. It is necessary to generate multiple OAMs in a single optical beam to increase the data transfer capacity. Efforts have been made to generate multiple OAMs in a single beam by an imprint of a helical phase of the superposition of multiple OAMs on the SLM (spatial light modulator) [8–11]. The advantage of SLM is that the multiple OAMs can be changed easily in the optical beam. However, SLMs cannot be used to generate multiple OAMs in the high power laser beams due to their low damage threshold. Recently, it is reported that using a spiral phase plate (SPP), the high power vortex beams can be generated [12]. Besides that, the SPPs convert Gaussian beam into a vortex beam with high conversion efficiency. The main drawback of SPPs is that they cannot be used to generate multiple OAMs in a single beam. However, by inserting the SPP in the Gaussian beam with phase singularity at off-axis with respect to the Gaussian beam axis, it is possible to generate multiple OAMs in the single beam [13–15]. It can be understood as follows: the off-axis Gaussian vortex beam (GVB) has the fractional OAM. The fractional OAM can be written as a superposition of integer OAMs. Recently several groups have shown that fractional OAM in the laser beams can be generated in different ways, viz; superposition of optical vortices [16], spiniform phase-encoded metagratings [17], off-axis SPP [18], non-integer phase step hologram on the SLM [19] and off-axis pumping of laser cavity [20]. In the above mentioned techniques, off-axis SPP is chosen because it provides the high optical power fractional OAM beam which is required for nonlinear wave-mixing. In addition, the off-axis vortex

beam with a single helical phase has stable propagation dynamics. In nonlinear wave-mixing, one has to focus the laser beam to increase the nonlinear efficiency. Under focusing condition, off-axis GVB preserves its shape throughout the propagation. The propagation dynamics of focused off-axis vortex beam is well-studied in the [21]. In the present work, first we characterize the off-axis GVB and show the generation of multiple OAMs in a single optical beam using a single helical phase structure introduced in the laser beams by off-axis SPP. Off-axis GVBs have a wide range of applications in the light-science [22–29]. Our discussions on the properties of symmetric and off-axis GVB provides additional knowledge to well utilize the off-axis GVB in the wide range of applications. The broad OAM spectra generated using the off-axis of a single helical phase structure can be utilized for optical communication [30–32].

On the other side, the wavelength of the optical beams plays a key role in information processing [33–35]. For any particular practical application, desired wavelength of optical beam cannot be directly achieved by laser sources due to their limitations [36]. The addition of nonlinear wave mixing to the lasers, one can generate OAM in the desired wavelength. In the present work, 1064 nm wavelength laser beam is considered as fundamental source for off-axis vortex beam generation. In the Second harmonic generation (SHG) process, the fundamental OAMs will be added to generate new OAM modes at 532 nm wavelength. Here, we propose type-II SHG of fundamental OAM modes to generate controlled OAM spectra at new wavelength. This paper is organized as follows: section 2 provides a brief explanation of off-axis GVB properties. In section 3, we provide a theoretical framework for type-II SHG of off-axis GVB. In section 4, we propose an experimental setup for polarization controlled OAM spectra generation through type-II SHG process. Section 5 describes the results of broad OAM spectra generation at fundamental as well as at SHG wavelength. Finally, we concluded our results in section 6.

2. Gaussian vortex beam and its off-axis characteristics

Gaussian vortex beams (GVBs) are zero radial index Laguerre–Gaussian beams (LG_0^l). Among all structured OAM beams, GVB is the most successfully used in the OAM based optical communication [35, 37] due to its simple transverse profile and also it is easy to control the mode structure for applications [38]. The Gaussian vortex beam with plane wave-front in terms of its radial (r) and azimuthal (θ) coordinates has the amplitude in the form of $E(r,\ \theta) = E_0(r/w)^l \exp(-r^2/w^2)\exp(il\theta)$, where, w is Gaussian beam spot size, l is OAM quantum number, and E_0 is an optical field amplitude. While, the normalized wave function of optical beam gives the optical field amplitude distribution as a function of radial coordinate, the square of the normalized wave function provides the intensity distribution of the optical field in the beam cross-section. The optical field amplitude and its intensity of plane wave-front GVB with azimuthal index (OAM), l can be written as

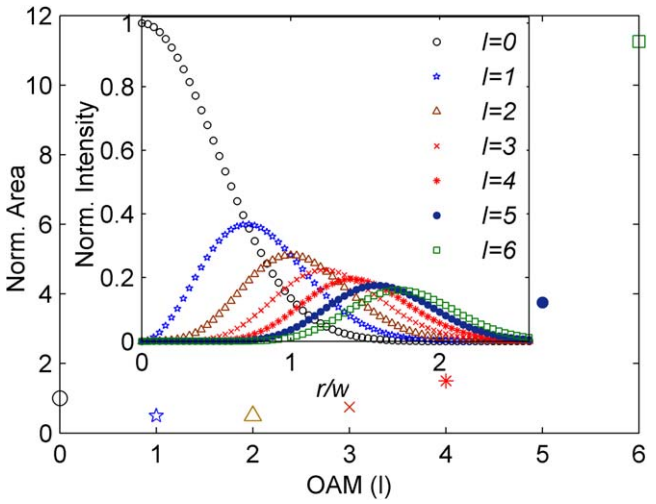

Figure 1. Normalized area of GVB as a function of OAM. Inset: line profile of GVB in terms of r/w; w is Gaussian beam spot size.

$$E_l(r,\ \theta) = \sqrt{\frac{2^l P}{n_0 \varepsilon_0 c l! \pi w^2}} \left[\frac{r}{w}\right]^l e^{\frac{-r^2}{w^2}} e^{-il\theta}, \tag{1a}$$

$$I_l(r) = \frac{2^l P}{n_0 \varepsilon_0 c l! \pi w^2} \left[\frac{r^2}{w^2}\right]^l e^{\frac{-2r^2}{w^2}}, \tag{1b}$$

here, P is the optical power within the laser beam, n_0 is refractive index, c is the velocity of light, and ε_0 is free space permittivity. As depicted in figure 1, the area of GVB is normalized with Gaussian beam area (zeroth order of GVB, $l = 0$) and plotted as a function of OAM order. The area of GVB rely on the content of OAM present in the beam and is given by $A_l = l!\pi w^2/2^{l+1}$. The area of vortex beam for orders, $l = 1$ and 2 are equal and $1/2$ times less than the Gaussian beam area and for order 3, it is $3/4$ times less than the Gaussian beam area. For all $l > 3$, the area of GVB increases with the order of GVB (l). In general, the increase in the cross-sectional area of the optical beams decreases their peak intensity, however, as shown in the inset of figure 1, even though the area of GVB for $l = 1$, 2 and 3 is less than other orders, $l = 0$ and $l > 0$, the peak intensity of GVB is decreasing as the order increased. This scenario can be expected from equation (1b) due to the peak intensity of GVB is constrained by two radial functions: Gaussian function $[\exp(-2r^2/w^2)]$ and singular function $[(r/w)^{2l}]$. The radius of GVB increases with its order [39] and the Gaussian profile exponentially decays as a function of radial coordinate in the same way for all orders of GVB. Hence, the peak intensity of GVB decreasing with increasing its order. All nonlinear wave-mixing processes are intensity dependent and their efficiency increases with increasing the peak intensity of interacting beams. In the nonlinear wave mixing of vortex beams, the efficiency of nonlinear wave-mixing decreases with increasing the GVB order due to the decrease in its peak intensity [12]. However, the nonlinear wave mixings have the following two advantages: the newly generated optical beam has the OAM either equal or higher than the pump beam

OAM [40–42] and it leads to control the OAM. Using nonlinear wave mixing one can generate GVB in the desired wavelength. In recent studies it is shown that using nonlinear wave mixing, OAM beams can be generated in the ultraviolet, mid-infrared, far-infrared and terahertz wavelength regions [41–45] where diffractive optical elements are not available to directly generate OAM beams.

The GVB is characterized by its OAM order and the OAM depends on the position of the phase singularity. The displacement of a singular point with respect to the Gaussian beam centre creates the off-axis GVB. In order to quantify the off-axis GVB, one has to parameterize the off-axis position with respect to the host beam (Gaussian beam) of the vortex. The off-axis GVB singular position can be quantitatively parameterized by off-axis (asymmetric) parameter $\gamma = r_0/w$, here, r_0 is the off-axis position of the vortex centre with respect to the Gaussian beam centre. The optical field amplitude and intensity distribution of off-axis GVB for OAM order, l and off-axis position (r_0, θ_0) are given by equation (2).

$$E_l(r, \theta) = \frac{\sqrt{P}}{\sqrt{2n_0\varepsilon_0 cA_l}}\left[\frac{re^{i\phi} - r_0e^{i\theta_0}}{w}\right]^l e^{\frac{-r^2}{w^2}}e^{-il\phi}, \quad (2a)$$

$$\mathrm{I}_l(r, \theta) = \frac{P}{2n_0\varepsilon_0 cA_l}\left[\frac{r^2 + r_0^2 - 2rr_0\cos(\theta - \theta_0)}{w^2}\right]^l e^{\frac{-2r^2}{w^2}}, \quad (2b)$$

here, A_l is *an* area of off-axis GVB. Expressions for the area of off-axis GVB for $l = 1$ to 6 are given by equations (3a)–(3f).

$$A_1 = \frac{\pi w^2}{4} + \frac{\pi r_0^2}{2}, \quad (3a)$$

$$A_2 = \pi\left[\frac{w^2}{4} + r_0^2 + \frac{r_0^4}{2w^2}\right], \quad (3b)$$

$$A_3 = \pi\left[\frac{3w^2}{8} + \frac{5r_0^2}{2} + \frac{5r_0^4}{2w^2} + \frac{r_0^6}{2w^4}\right], \quad (3c)$$

$$A_4 = \pi\left[\frac{3w^2}{4} + 6r_0^2 + \frac{9r_0^4}{w^2} + \frac{4r_0^6}{w^4} + \frac{r_0^8}{2w^6}\right], \quad (3d)$$

$$A_5 = \pi\left[\frac{15w^2}{8} + \frac{21r_0^2}{2} + \frac{153r_0^4}{8w^2} + \frac{51r_0^6}{4w^4} + \frac{7r_0^8}{2w^6} + \frac{r_0^{10}}{2w^8}\right], \quad (3e)$$

$$A_6 = \pi\left[\frac{45w^2}{8} + \frac{45r_0^2}{4} + \frac{99r_0^4}{4w^2} + \frac{246r_0^6}{4w^4} + \frac{99r_0^8}{4w^6} + \frac{9r_0^{10}}{2w^8} + \frac{r_0^{12}}{2w^{10}}\right], \quad (3f)$$

Off-axis GVB properties for OAM, $l = 0$–6 are presented in figure 2. As depicted in figure 2(*a*), the area of off-axis GVB increases with the off-axis parameter (γ). Here, the off-axis GVB area is normalized with the Gaussian beam area to standardize the change in the off-axis GVB area as a function of γ. The area of GVB is a convolution of an area of vortex function, r/w, and Gaussian function, $\exp(-r^2/w^2)$. The

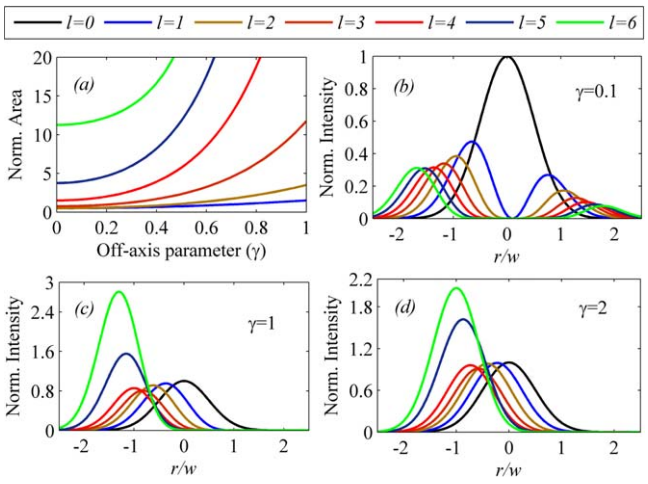

Figure 2. Off-axis GVB properties: (a) normalized area of off-axis GVB as a function of off-axis parameter for $l = 1$ to 6; (b), (c), and (d) are line profiles of off-axis GVB along the phase singularity point displacement for respective off-axis parameter values $\gamma = 0.1$, 1, and 2.

combined area of two functions is given by convolution integral of them. The convolution area of the two functions increasing with increasing the separation of their centers. Hence, for a given OAM, the area of off-axis GVB increases with an increase in γ due to the increase in the separation between the two functions. The contribution of r_0 in this scenario can be understood in equation (3). Further, the change in the area of off-axis GVB with respect to γ is increasing with the order of the vortex due to the increase in the area of vortex beam. It can be understood as: with increasing the order of the vortex, the number of higher order terms of r_0 increasing in the vortex beam area. Figures 2(b)–(d) correspond to normalized peak intensity line profile of off-axis GVB for OAM, $l = 0$ to 6 along the phase singular point displacement for respective $\gamma = 0.1$, 1 and 2. The intensity of off-axis GVB line profile is normalized with peak intensity of Gaussian beam. The shift in the phase singular position decreases the peak intensity of GVB along the shift direction and simultaneously increases its peak intensity in the opposite direction. As depicted in figure 2(b), in the presence of small shifts of phase singular point, the maximum peak intensity of GVB for all OAMs is smaller than the Gaussian beam peak intensity. As shown in figure 2(c), at phase singular point shifts close to the beam spot size, the peak intensity of GVB of order $l = 1$–4 is smaller than the Gaussian beam peak intensity. For $l > 4$, the GVB peak intensity is larger than the Gaussian profile peak intensity. This kind of behavior can be expected for higher order vortex beams due to their large dark core size with respect to Gaussian beam spot size and vortex ring width decreasing with increasing its order. The shift in the phase singular point of higher order vortex beam redistributes the ring shape intensity into a crescent shape and it leads to the increase in the peak intensity which is higher than the Gaussian peak intensity. Further increase in the displacement of phase singular point position decreases the peak intensity of off-axis vortex beam and this behavior can be

seen in figures 2(c) and (d) due to an increase in the width of vortex crescent. Further increase in the phase singular point shift leads to the Gaussian shape for all vortex beams and as a result vortex peak intensity converges to Gaussian beam peak intensity. In the nonlinear wave mixing, the advantage of off-axis GVB over symmetric GVB is that the off-axis vortex beams with broad OAM spectra have the larger nonlinear conversion efficiency than the single OAM vortex beams due to high peak intensity of off-axis vortex beams as compared with symmetric vortex beams. Thus, we can tune the wavelength of broad OAM spectra with high conversion efficiency as compared with single OAM modes.

The off-axis GVBs sees the less helical phase of diffractive optical element as compared with their on-axis phase singular vortex beams (symmetric GVBs). Thus the off-axis vortex beam can have the fractional OAM and is always less than its symmetric vortex beam OAM. One can obtain the OAM content of off-axis GVBs as a function of their off-axis parameter (γ) [21]. The fractional OAM can be written in terms of integer OAM basis as [46]

$$P_n(l'SA) = \frac{\sin^2(\mu\pi)}{(l' - n)^2\pi^2}, \tag{4}$$

here, l' is fractional OAM, n is integer OAM, and $\mu\epsilon[0, 1)$.

3. Second harmonic generation of Off-Axis Gaussian vortex beam

The nonlinear wave mixing of GVB takes place in the nonlinear medium is the same way as the nonlinear wave mixing of Gaussian beam. In the nonlinear wave mixing of GVB, in addition to energy and momentum conservation, the nonlinear process has to satisfy the OAM conservation. The type-I second harmonic generation of off-axis GVB is already studied both theoretically and experimentally in [13]. To study the collinear type-II SHG of GVB, let us assume that the fundamental GVBs with OAMs, l_1 and l_2 are polarized in the horizontal and vertical direction to achieve the phase matching for the second harmonic GVB with OAM l_3, which is polarized in the vertical direction. The interacting optical beam's propagation direction is considered in the z-direction. The optical amplitude equations of off-axis GVB for fundamentals and second harmonic beams are given by equation 5.

$$\mathrm{E}^h_{l_1}(r, z, t) = \mathrm{E}^h_0\left(\frac{r - r_1}{w_\omega}\right)^{l_1} e^{\frac{-r^2}{w^2}} e^{-il_1\phi} e^{i(k^h_\omega z - \omega t)}\widehat{h}, \tag{5a}$$

$$\mathrm{E}^v_{l_2}(r, z, t) = \mathrm{E}^v_0\left(\frac{r - r_2}{w_\omega}\right)^{l_2} e^{\frac{-r^2}{w^2}} e^{-il_2\phi} e^{i(k^v_\omega z - \omega t)}\widehat{v}, \tag{5b}$$

$$\mathrm{E}^v_{l_3}(r, z, t) = \mathrm{E}^v_0\left(\frac{r - r_3}{w_{2\omega}}\right)^{l_3} e^{\frac{-r^2}{w^2}} e^{-il_3\phi} e^{i(k^v_{2\omega} z - 2\omega t)}\widehat{v}, \tag{5c}$$

here, w_ω and $w_{2\omega}$ are spot sizes of fundamental and second harmonic beams, respectively. r_1, r_2, and r_3 are the position of phase singular points of fundamental-1, fundamental-2 and SHG signal respectively. Energy, momentum and OAM conservation conditions of SHG are $\omega + \omega = 2\omega$, $k^v_\omega + k^h_\omega = k^v_{2\omega}$, and $l_1 + l_2 = l_3$ respectively. The equation of propagation for the type-II second harmonic field in terms of fundamental fields is given by

$$\nabla^2\mathrm{E}^v_{l_3} - \frac{n^2_{2\omega}}{c^2}\frac{\partial^2\mathrm{E}^v_{l_3}}{\partial t^2} = \frac{\chi^{(2)}}{c^2}\frac{\partial^2(\mathrm{E}^h_{l_1}\mathrm{E}^v_{l_2})}{\partial t^2}. \tag{6}$$

By solving equation (6) in the presence of lossless media and under slowly varying amplitude approximation, we can obtain the differential equation for second harmonic beam in terms of fundamental optical amplitudes as [47]

$$\frac{\partial\mathrm{E}^v_{l_3}}{\partial z} = ig\Gamma^{(l_3l_1l_2)}\mathrm{E}^h_0\mathrm{E}^v_0 e^{i\Delta kz} e^{i(l_1+l_2-l_3)\phi}. \tag{7}$$

The g and spatial overlapping function $\Gamma^{(l_3l_1l_2)}$ of the fundamental and SHG beams are

$$g = \frac{\chi^{(2)}}{2c}\sqrt{\frac{2\omega^3}{n^v_\omega n^h_\omega n_{2\omega}}}R^{000}, \tag{8}$$

$$\Gamma^{(l_3l_1l_2)} = \frac{R^{l_3l_1l_2}}{R^{000}}. \tag{9}$$

The LG^l_0 modes construct a complete and orthonormal basis. Hence, the fractional OAM of off-axis GVB can be written as a superposition of integer OAMs in their integer basis. The optical fields of off-axis GVB can be written as sum of the symmetrical optical vortex field amplitudes. Therefore, the fundamental and SHG off-axis GVBs in their integer basis are given by equations (9a)–(9c).

$$\mathrm{E}^h_{l_1}(r, z, t) = \sum_{n_1=-\infty}^{\infty}\mathrm{E}_{n_1}\left(\frac{r}{w_\omega}\right)^{n_1} e^{-in_1\phi} e^{(-r^2/w_\omega{}^2)} e^{i(k^h_\omega z - \omega t)}\widehat{h}, \tag{9a}$$

$$\mathrm{E}^v_{l_2}(r, z, t) = \sum_{n_2=-\infty}^{\infty}\mathrm{E}_{n_2}\left(\frac{r}{w_\omega}\right)^{n_2} e^{-in_2\phi} e^{(-r^2/w_\omega{}^2)} e^{i(k^v_\omega z - \omega t)}\widehat{v}, \tag{9b}$$

$$\mathrm{E}^v_{l_3}(r, z, t) = \sum_{n_3=-\infty}^{\infty}\mathrm{E}_{n_3}\left(\frac{r}{w_{2\omega}}\right)^{n_3} e^{-in_3\phi} e^{(-r^2/w_{2\omega}{}^2)} e^{i(k^v_{2\omega} z - 2\omega t)}\widehat{v}, \tag{9c}$$

here, n_1, n_2, and n_3 are integer OAMs in the Hilbert-space. The spatial overlapping of symmetrical vortex field amplitudes of the two fundamental beams and SHG beam is

$$R^{l_3l_1l_2} = \int_{r=0}^{\infty}\int_{\varphi=0}^{2\pi}\sum_{n_1=-\infty}^{\infty}\sum_{n_2=-\infty}^{\infty}\sum_{n_3=-\infty}^{\infty}\left(\frac{r}{w_\omega}\right)^{n_1+n_2}\left(\frac{r}{w_{2\omega}}\right)^{n_3} \times e^{-r^2(2/w_\omega{}^2+1/w_{2\omega}{}^2)} e^{i(n_1+n_2-n_3)\phi} r dr d\varphi\delta_{n_3,n_1+n_2}. \tag{10}$$

The overlapping integral will be zero for $n_1 + n_2 \neq n_3$. Thus, the number of OAM modes generated in the SHG from the fundamental OAM modes interaction is constrained by spatial overlap integral.

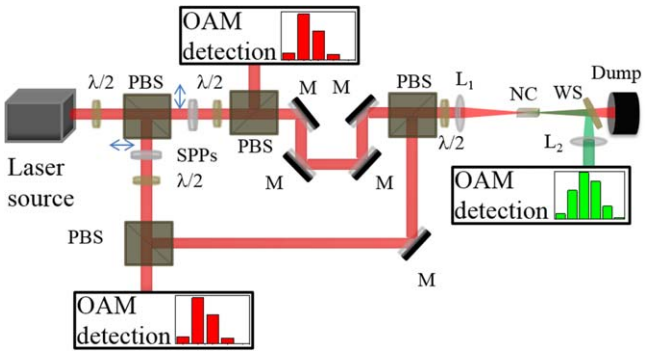

Figure 3. Schematic of an experimental setup for simultaneous generation of controlled broad OAM spectra in two wavelengths (fundamental and SHG): $\lambda/2$, half-wave plate; PBS, polarizing beam splitter cube; SPP, spiral phase plate; M, mirrors; Dump, power dumper; NC, nonlinear crystal; WS, wavelength separator.

4. Proposed experimental setup

The schematic of proposed experimental setup for simultaneous generation of controlled broad OAM spectra at fundamental wavelength as well as at second harmonic wavelength is given in figure 3. In experimental diagram as well as in OAM spectra data, we have given red colour for pump/fundamental wavelength and green colour for SHG wavelength for clear understanding of proposed experimental setup. To generate polarization controlled OAM spectra in the pump as well as in SHG, first, we have to pass the linearly polarized fundamental beam through a set of half-wave plate ($\lambda/2$) and a polarizing beam splitter to split into two beams. Using half-wave plate, we can control the optical power in each arm and can call it as a power-controlled $\lambda/2$ plate. The transmitted (fundamental-1) and reflected (fundamental-2) beams can pass through two different topological charged SPPs. Let us assume that the OAM generated in the fundamental-1 and fundamental-2 are l_1 and l_2 respectively. As discussed in the theory, to generate broad OAM spectra in the fundamental beams, one must mount the SPPs on the transitional stages to control their off-axis position. Using off-axis parameter $\gamma = r_0/w_S$, we can control the OAM spectra generated in each optical beam. Here, w_S and r_0 are the Gaussian beam spot size at SPP and off-axis position of SPP respectively. Another combination of half-wave plate and polarizing beam splitter can be used in each of the two arms to further divide each beam into two parts. In that one part is for detection of OAM content in each pump and another part for the SHG process. The generated OAM spectra in the laser beams can be detected using different techniques [48–53]. In the case of a pulsed laser beam, the delay stage in the fundamental-1 has to be used to obtain a perfect temporal overlap of two fundamental beams. Two fundamental beams can be collinearly overlapped using the fourth PBS. Lens, L_1 can be used to focus the input beams into the nonlinear crystal (NC) and lens L_2 can be used to collimate the SHG beam which is separated from the pump through the wavelength separator (WS). The polarization phase matching of a nonlinear crystal, NC can be controlled using a half-wave plate, which is kept after fourth PBS and let it is named as a phase-matching controlled $\lambda/2$ plate.

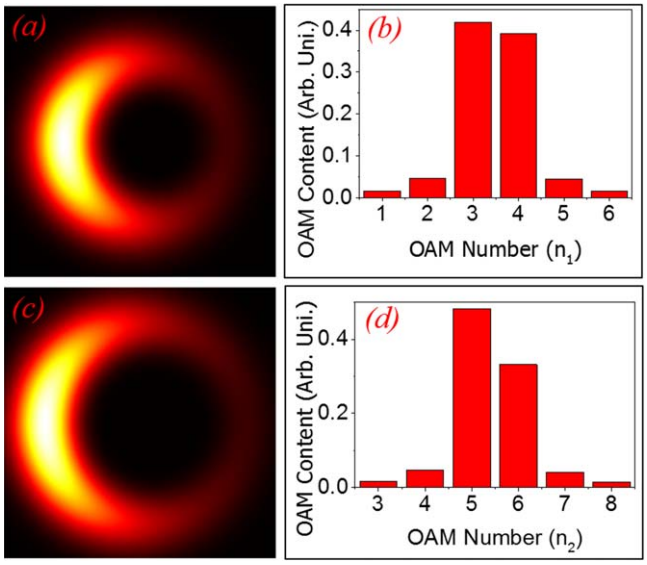

Figure 4. Fundamental vortex beams: Fundamental-1 vortex beam (*a*) transverse intensity distribution and its (*b*) OAM content; Fundamental-2vortex beam (*c*) transverse intensity distribution and its (*d*) OAM content.

5. Results and discussions

The off-axis fundamental GVB characteristics are depicted in figure 4. We have chosen GVB of OAM order $l_1 = 4$ as fundamental-1. For off-axis parameter value, $\gamma = 0.3$, the OAM contained in the beam become $l_1 = 3.5$ instead of $l_1 = 4$. Figure 4(a) shows the cross-sectional intensity distribution of fundamental-1. The transverse intensity distribution of vortex becomes asymmetric due to the off-axis of the vortex phase singularity with respect to Gaussian profile centre. As we mathematically explained in equation (4), the fractional OAM contained in the off-axis fundamental-1 can be written as super-position of integer OAMs. The OAMs in the fundamental-1 are distributed in the range of integer OAMs, $n_1 = 1$–6. The OAM spectra for $\gamma = 0.3$ is shown in figure 4(b). While the OAM content dominant at $n_1 = 3$ and 4, its minimal content present on either side of central maximum of OAM spectra. With increasing the off-axis parameter value, the fractional OAM content decreases [13] and as a result, the central maximum of OAM spectra moves to lower integer values of OAM. The superposition state of OAM spectra collapses into the zero OAM state for $\gamma \gg 1$ and the crescent intensity distribution of off-axis GVB becomes Gaussian intensity distribution. The OAM of fundamental-2 is considered as $l_2 = 6$. As like in fundamental-1, we have given shift in the phase singularity of vortex beam with off-axis parameter value, $\gamma = 0.2$. As a result, the OAM contained in the fundamental-2 beam is $l_2 = 5.4$. The cross-sectional intensity distribution of fundamental-2 is shown in figure 4(c). The OAM modes generated in the fundamental-2 due to off-axis of phase singular point are distributed in the

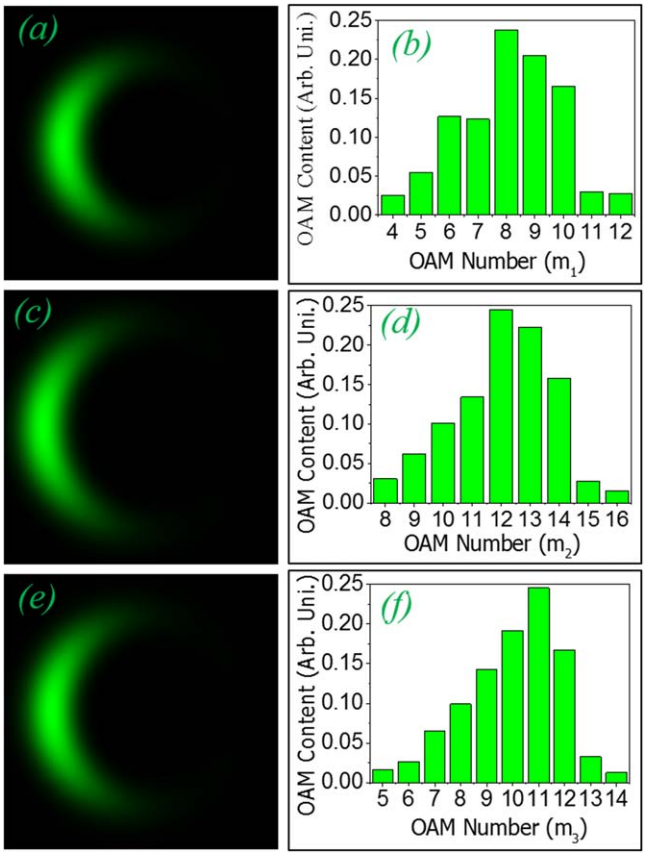

Figure 5. (a), (c) and (e) are cross-sectional intensity distribution of type-II SHG and corresponding OAM spectra are (b), (d) and (f) generated using polarization control:(a), (b) SHG of fundamental-1, power-controlled $\lambda/2$ plate angle, $\alpha_1 = 0^\circ$ and phase-matching $\lambda/2$ plate angle, $\alpha_2 = 22.5^\circ$; (c), (d) SHG of fundamental-2, power-controlled $\lambda/2$ plate angle, $\alpha_1 = 45^\circ$ and phase-matching $\lambda/2$ plate angle, $\alpha_2 = 22.5^\circ$; (e), (f) SHG of fundamental-1and fundamental-2, power-controlled $\lambda/2$ plate angle, $\alpha_1 = 22.5^\circ$ and phase-matching $\lambda/2$ plate angle, $\alpha_2 = 0^\circ$.

range of integer OAMs, $n_1 = 3$–8. The OAM modes distribution in the integer basis is depicted in figure 4(d). The maximum OAM content present at $n_1 = 5$ and 6. The optical power in the OAM spectra of each fundamental beam can be controlled using a power-controlled $\lambda/2$ plate.

Type-II SHG characteristics of fundamental OAMs discussed in figure 4 are presented in figure 5. The polarization controlled OAM spectra at second harmonic wavelength can be generated using a power-controlled $\lambda/2$ plate and phase-matching controlled $\lambda/2$ plate. The cross-sectional intensity of the SHG beam and its OAM spectra are obtained from equations (7)–(10). We assume that the laser is delivering optical power with horizontal polarization. The angle of power-controlled $\lambda/2$ plate (α_1) and phase-matching controlled $\lambda/2$ plate (α_2) are with respect to horizontal axis (i.e., optic axis angle of $\lambda/2$ plate is 0° when it is along horizontal direction). The SHG of fundamental-1 OAM spectra can be obtained in the designed experimental setup as follows: the power-controlled $\lambda/2$ plate at an angle $\alpha_1 = 0^\circ$ will not rotate the horizontal polarization. The PBS allows the entire power in the fundamental-1 arm and power in the fundamental-2 arm will be zero. The phase-matching controlled $\lambda/2$ plate at an angle $\alpha_2 = 22.5^\circ$ provides the equal projections of fundamental-1 beam in the horizontal and vertical direction for type-II SHG. Figure 5(a) is the transverse intensity distribution of SHG signal generated from the fundamental-1. SHG is an intensity dependent process, as a result the asymmetry in the vortex intensity distribution increased in the SHG beam from the fundamental beam. The OAM content of SHG beam is presented in figure 5(b). The fundamental OAM spectra distributed in the range $n_1 = 1$–6 is transformed into the OAM spectra range of $m_1 = 4$–12 in the SHG signal. The range of OAM spectra at SHG wavelength is larger than the corresponding fundamental beam OAM spectra due to the property of individual OAM modes addition in the SHG process. The spatial overlapping of fundamental and SHG modes leads the centre of the SHG OAM spectra at $m_1 = 8$ for fundamental-1 beam OAM spectra centre at $n_1 = 3$. Similar way, we can generate the OAM spectra at SHG wavelength for fundamental-2 beam by rotating the polarization of laser beam in the vertical direction through the power-controlled $\lambda/2$ plate at an angle $\alpha_1 = 45^\circ$ while not changing the phase-matching controlled $\lambda/2$ plate angle, $\alpha_2 = 22.5^\circ$. The transverse intensity distribution of SHG signal generated from the fundamental-2 beam is depicted in figure 5(c). The spatial mode size of fundamental-2 SHG signal is larger than the fundamental-1 SHG signal due to the presence of higher order OAM modes. The OAM spectra distribution of fundamental-2 SHG is illustrated in figure 5(d). In the SHG of fundamental-2, the fundamental OAM spectra range of $n_2 = 3$–8 in the integer OAM basis is shifted to $m_2 = 8$–16. The SHG OAM spectra have peaked at $m_2 = 12$ for fundamental-2 spectra peak at $n_2 = 5$. The addition of OAMs of two fundamental beams can be obtained by splitting the pump power into two equal optical powers in the two arms at first PBS by keeping the power-controlled $\lambda/2$ plate at an angle $\alpha_1 = 22.5^\circ$. The phase-matching controlled $\lambda/2$ plate has to be at $\alpha_2 = 0^\circ$ to generate the SHG signal from the two fundamental beams. Figure 5(e) illustrates the transverse intensity distribution of the SHG signal generated from the fundamentals of 1 and 2. In this case, the spatial profile is larger than the fundamental-1 SHG and smaller than the fundamental-2 SHG due to the spatial overlap integral of two fundamental spatial profiles in the SHG process. As shown in figure (f), the generated OAM spectra at SHG wavelength is in the range of $m_3 = 5$–14. The SHG OAM spectra have peaked at $m_3 = 11$ for fundamental-1 beam OAM spectra centre at $n_1 = 3$ and fundamental-2 spectra centre at $n_2 = 5$. The range and position of polarization controlled OAM spectra generated in the above three cases can be tuned by tuning the fundamental OAM spectra through the off-axis parameter, γ. The range of OAM spectra can further increase by cascade SHG process.

In addition to generate polarization controlled OAM spectra at SHG wavelength, we can generate a broad range of OAM spectra at SHG wavelength through the superposition of more than one SHG mode generated by SHG process. In the type-II SHG, we can generate simultaneously more than one spatial mode at SHG wavelength through the phase-

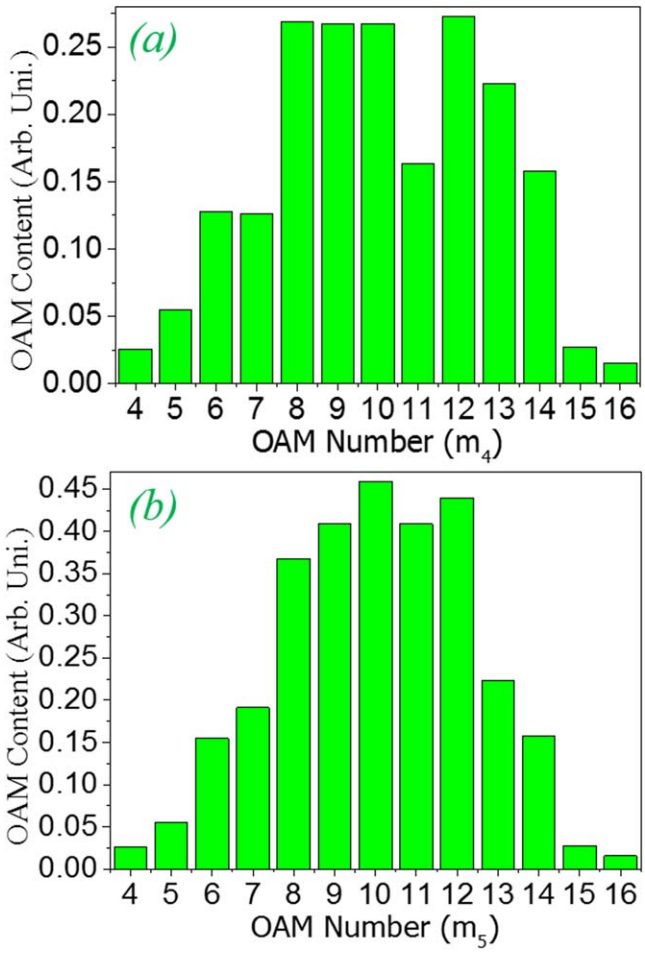

Figure 6. Polarization controlled broad OAM spectra generation at SHG wavelength: (*a*) power-controlled $\lambda/2$ plate angle, $\alpha_1 = 22.5^0$ and phase-matching $\lambda/2$ plate angle, $\alpha_2 = 22.5^0$ and (*b*) power-controlled $\lambda/2$ plate angle, $\alpha_1 = 22.5^0$ and phase-matching $\lambda/2$ plate angle, $\alpha_2 = 11.25^0$.

matching controlled $\lambda/2$ plate [54]. Figure 6 depicts the OAM spectra for two angles of the phase-matching controlled $\lambda/2$ plate. By keeping the power-controlled $\lambda/2$ plate at $\alpha_1 = 22.5°$ and phase-matching controlled $\lambda/2$ plate at $\alpha_2 = 22.5°$, we can generate two spatial modes at SHG wavelength. The phase-matching controlled $\lambda/2$ plate at an angle $\alpha_2 = 22.5°$ rotates the two orthogonal polarizations (fundamental modes) at 45°. Hence the two fundamental modes have equal projections on horizontal and vertical axes. Thus, we can simultaneously generate coherent superposition of SHG of fundamental-1 mode (discussed in figures 5(a)–(b)) and SHG of fundamental-2 mode (discussed in figures 5(c), (d)). The SHG OAM spectra is presented in figure 6(a). The wide range OAM spectra ($m_4 = 4$–16) generated and also increased the OAM modes weight. Similar way we can generate the superposition of three SHG modes discussed in figure 5 in the presence of power-controlled $\lambda/2$ plate at $\alpha_1 = 22.5°$ and phase-matching controlled $\lambda/2$ plate at $\alpha k_2 = 11.25°$. The phase-matching controlled $\lambda/2$ plate at an angle $\alpha_2 = 11.25^0$ rotates the two orthogonal polarizations (fundamental modes) at 22.5^0. As a result, the fundamental modes amplitude projections on horizontal and vertical axes are unequal and it leads to the self- as well as mutual-SHG of two fundamental modes. The OAM spectra of coherent superposition of three modes is shown in figure 6(b). The range of OAM spectra for superposition of three modes is same as two modes superposition but the distribution of OAM spectra is different. Using a continuous variation of phase-matching $\lambda/2$ plate angle, we can further tune the OAM modes distribution in the OAM spectra. Using three parameters: off-axis parameter, power controlled $\lambda/2$ plate angle, and phase-matching controlled $\lambda/2$ plate angle, we can control the peak position, distribution and range of OAM spectra.

6. Conclusion

We have derived theoretical equations for off-axis GVB and characterized its properties. The increase in the peak intensity of off-axis GVB with its off-axis parameter confirms that the nonlinear wave mixing efficiency of off-axis GVB is larger than the symmetric GVB. As a result, the SHG efficiency of multiple OAMs is larger than the SHG efficiency of single OAM. Using multiple OAMs of off-axis GVB, we have demonstrated the polarization controlled OAM spectra in the fundamental wavelength as well as in the second harmonic wavelength in the presence of two $\lambda/2$ plates: power-controlled $\lambda/2$ plate and phase-matching controlled $\lambda/2$ plate. The individual addition of integer OAMs of fundamental beams in the SHG process allows us to generate a wide range of OAM spectra at second harmonic wavelength. Using our proposed method, we can easily control the range, peak position, and distribution of OAM spectra. Also, we can tune the wavelength of single helical phase OAM spectra to desire application with high nonlinear conversion efficiency.

ORCID iDs

A Srinivasa Rao https://orcid.org/0000-0001-6247-2546

References

[1] Allen L, Beijersbergen M W, Spreeuw R J C and Woerdman J P 1992 Orbital angular momentum of light and the transformation of Laguerre–Gaussian laser modes *Phys. Rev. A* **45** 8185
[2] Barreiro J T, Weiand T C and Kwiat P G 2008 Beating the channel capacity limit for linear photonic super dense coding *Nature Phys.* **4** 282
[3] Williams B P, Sadlier R J and Humble T S 2017 Super dense coding over optical fibre links with complete Bell-state measurements *Phys. Rev. Lett.* **118** 050501
[4] Braunstein S L and Kimble Dense H J 2000 coding for continuous variables *Quantum Information with Continuous Variables* pp 95–103(Dordrecht: Springer)
[5] Leach J, Bolduc E, Gauthier D J and Boyd R W 2012 Secure information capacity of photons entangled in many dimensions *Phys. Rev. A* **85** 060304
[6] Flamini F, Spagnolo N and Sciarrino F 2018 hotonic quantum information processing: a review *Rep. Pro. Phys.* **82** 016001

[7] Mi S, Wang T J, Jin G S and Wang C 2015 High-capacity quantum secure direct communication with orbital angular momentum of photons *IEEE Phot. J.* **7** 1–8

[8] Fu S, Zhang S, Wang T and Gao C 2016 Measurement of orbital angular momentum spectra of multiplexing optical vortices *Opt. Exp.* **24** 6240–8

[9] Yao E, Franke-Arnold S, Courtial J, Barnett S and Padgett M 2006 Fourier relationship between angular position and optical orbital angular momentum *Opt. Exp.* **14** 9071–6

[10] Xiao Q, Klitis C, Li S, Chen Y, Cai X, Sorel M and Yu S 2016 Generation of photonic orbital angular momentum superposition states using vortex beam emitters with superimposed gratings *Opt. Exp.* **24** 3168–76

[11] Liu Y D, Gao C, Qi X and Weber H 2008 Orbital angular momentum (OAM) spectrum correction in free space optical communication *Opt. Exp.* **16** 7091–101

[12] Chaitanya N A, Aadhi A, Jabir M V and Samanta G K 2015 Frequency-doubling characteristics of high-power, ultrafast vortex beams *Opt. Lett.* **40** 2614–7

[13] Alam S U, Rao A S, Ghosh A, Vaity P and Samanta G K 2018 Nonlinear frequency doubling characteristics of asymmetric vortices of tunable, broad orbital angular momentum spectrum *Appl. Phys. Lett.* **112** 171102

[14] Chu J, Chu D and Smithwitck Q 2017 Off-axis points encoding/decoding with orbital angular momentum spectrum *Sci. Rep.* **7** 43757

[15] Vasnetsov M V, Pas' Ko V A and Soskin M S 2005 Analysis of orbital angular momentum of a misaligned optical beam *New J. Phys.* **7** 46

[16] Kotlyar V V, Kovalev A A and Porfirev A P 2019 Calculation of fractional orbital angular momentum of superpositions of optical vortices by intensity moments *Opt. Exp.* **27** 11236–51

[17] Huang K, Liu H, Restuccia S, Mehmood M Q, Mei S T, Giovannini D, Danner A, Padgett M J, Teng J H and Qiu C W 2018 Spiniform phase-encoded metagratings entangling arbitrary rational-order orbital angular momentum *Light: Sci. Appl.* **7** 17156

[18] Kotlyar V, Kovalev A, Porfirev A and Kozlova E 2019 Orbital angular momentum of a laser beam behind an off-axis spiral phase plate *Opt. Lett.* **44** 3673–6

[19] Götte J B, O'Holleran K, Preece D, Flossmann F, Franke-Arnold S, Barnett S M and Padgett M J 2008 Light beams with fractional orbital angular momentum and their vortex structure *Opt. Exp.* **16** 993–1006

[20] Hsieh Y H, Lai Y H, Hsieh M X, Huang K F and Chen Y F 2018 Generating high-power asymmetrical Laguerre–Gaussian modes and exploring topological charges distribution *Opt. Exp.* **26** 31738–49

[21] Kotlyar V V, Kovalev A A and Porfirev A P 2017 Asymmetric Gaussian optical vortex *Opt. Lett.* **42** 139–42

[22] Huang X, Xu B, Cui S, Xu H, Cai Z and Chen L 2018 Direct generation of vortex laser by rotating induced off-axis pumping *IEEE J. of Selected Topics in Quant. Electron.* **24** 1–6

[23] Bovino F A, Braccini M, Giardina M and Sibilia C 2011 Orbital angular momentum in noncollinear second-harmonic generation by off-axis vortex beams *JOSA B* **28** 2806–11

[24] Zhao X, Zhang J, Pang X and Wan G 2017 Properties of a strongly focused Gaussian beam with an off-axis vortex *Opt. Commun.* **389** 275–82

[25] Vasnetsov M V, Slyusar V V and Soskin M S 2001 Mode separator for a beam with an off-axis optical vortex *Quant. Electron.* **31** 464

[26] Pu Y and Meng H 2000 An advanced off-axis holographic particle image velocimetry (HPIV) system *Exp. Fluids* **29** 184–97

[27] Novoa D, Sola I J, García-March M A and Ferrando A 2014 The key role of off-axis singularities in free-space vortex transmutation *Appl. Phys. B* **116** 779–83

[28] Chen G, Huang X, Xu C, Huang L, Xie J and Deng D 2019 Propagation properties of autofocusing off-axis hollow vortex Gaussian beams in free space *Opt. Exp.* **27** 6357–69

[29] Guilleumas M and Graham R 2001 Off-axis vortices in trapped Bose-condensed gases: Angular momentum and frequency splitting *Phys. Rev. A* **64** 033607

[30] Yao A M and Padgett M J 2011 Orbital angular momentum: origins, behavior and applications *Adv. Opt. Photon.* **3** 161–204

[31] Li L *et al* Orbital-angular-momentum-multiplexed free-space optical communication link using transmitter lenses *Appl. Opt.* **55** 2098–1032016

[32] Malik M, Mirhosseini M, Lavery M P, Leach J, Padgett M J and Boyd R W 2014 Direct measurement of a 27-dimensional orbital-angular-momentum state vector *Nature commun.* **5** 3115

[33] Kim I I, McArthur B and Korevaar E J 2001 Comparison of laser beam propagation at 785 nm and 1550 nm in fog and haze for optical wireless communications *Optical Wireless Communications III.* (International Society for Optics and Photonics) vol. 4214, pp. 26–38

[34] Kedar D and Arnon S 2004 Urban optical wireless communication networks: the main challenges and possible solutions *IEEE Commun. Mag.* **42** S2–7

[35] Willner A E *et al* 2015 Optical communications using orbital angular momentum beams *Adv. Opt. Photon.* **7** 66–106

[36] Silfvast W T 2004 *Laser Fundamentals.* (Cambridge: Cambridge University Press)

[37] Wang J 2016 Advances in communications using optical vortices *Photon. Res.* **4** B14–28

[38] Zhang D, Feng X and Huang Y 2012 Encoding and decoding of orbital angular momentum for wireless optical interconnects on chip *Opt. Exp.* **20** 26986–95

[39] Reddy S G, Permangatt C, Prabhakar S, Anwar A, Banerji J and Singh R P 2015 Divergence of optical vortex beams *Appl. Opt.* **54** 6690–3

[40] Lenzini F, Residori S, Arecchi F T and Bortolozzo U 2011 Optical vortex interaction and generation via nonlinear wave mixing *Phys. Rev. A* **84** 061801

[41] Aadhi A and Samanta G K 2017 High-power, high repetition rate, tunable, ultrafast vortex beam in the near-infrared *J. Opt.* **20** 01LT01

[42] Chaitanya N A, Kumar S C, Devi K, Samanta G K and Ebrahim-Zadeh M 2016 Ultrafast optical vortex beam generation in the ultraviolet *Opt. Lett.* **41** 2715–8

[43] Aadhi A, Sharma V, Singh R P and Samanta G K 2017 Continuous-wave, singly resonant parametric oscillator-based mid-infrared optical vortex source *Opt. Lett.* **42** 3674–7

[44] He J, Wang X, Hu D, Ye J, Feng S, Kan Q and Zhang Y 2013 Generation and evolution of the terahertz vortex beam *Opt. Exp.* **21** 20230–9

[45] Neshev D N, Dreischuh A, Maleshkov G, Samoc M and Kivshar Y S 2010 Supercontinuum generation with optical vortices *Opt. Exp.* **18** 18368–73

[46] Götte J B, Franke-Arnold S, Zambrini R and Barnett S M 2007 Quantum formulation of fractional orbital angular momentum *J. Mod. Opt.* **54** 1723–38

[47] Pereira L J, Buono W T, Tasca D S, Dechoum K and Khoury A Z 2017 Orbital-angular-momentum mixing in type-II second-harmonic generation *Phys. Rev. A* **96** 053856

[48] Lavery M P, Berkhout G C, Courtial J and Padgett M J 2011 Measurement of the light orbital angular momentum spectrum using an optical geometric transformation *J. Opt.* **13** 064006

[49] Zhao P, Li S, Feng X, Cui K, Liu F, Zhang W and Huang Y 2017 Measuring the complex orbital angular momentum spectrum of light with a mode-matching method *Opt. Lett.* **42** 1080–3

[50] Leach J, Padgett M J, Barnett S M, Franke-Arnold S and Courtial J 2002 Measuring the orbital angular momentum of a single photon *Phys, Rev. Lett.* **88** 257901

[51] Ni B, Guo L, Yue C and Tang Z 2017 A novel measuring method for arbitrary optical vortex by three spiral spectra *Phys. Lett. A* **381** 817–20

[52] Mair A, Vaziri A, Weihs G and Zeilinger A 2001 Entanglement of the orbital angular momentum states of photons *Nat.* **412** 313

[53] Mirhosseini M, Malik M, Shi Z and Boyd R W 2013 Efficient separation of the orbital angular momentum eigenstates of light *Nature Commun.* **4** 2781

[54] Buono W T, Santiago J, Pereira L J, Tasca D S, Dechoum K and Khoury A Z 2018 Polarization-controlled orbital angular momentum switching in nonlinear wave mixing *Opt. Lett.* **43** 1439–42